Effect of Intermediate Heat Treatment on Microstructure and Texture Evolution of Continuous Cast Al-Mn-Mg Alloy Sheet

JIANTAO LIU, S.W. BANOVIC, R.J. FIELDS, and J.G. MORRIS

The microstructure and crystallographic texture evolution of continuous-cast, hot-rolled Al-Mn-Mg alloy sheet during cold rolling and subsequent annealing was investigated. All specimens cut from the as-received sheet were cold rolled and subsequently annealed, with some of these specimens receiving an intermediate heat treatment (IHT) prior to cold rolling. It was found that the degree of deformation and temperature of the annealing had a significant effect on the final grain size and texture of the sheet specimens, respectively. Furthermore, the IHT altered the development of the microstructure and texture of the final sheet specimens when compared to similarly produced specimens without it. For the sheet specimens without the IHT, a severely elongated grain structure was found in which the texture was dominated by a strong P orientation {011}<566>, despite the fact that the specimen was completely recrystallized. In contrast, specimens receiving the same cold rolling and annealing conditions but with the IHT had an equiaxed grain structure with a sharp Cube orientation {001}<100>. Counterbalancing the deformation textures from rolling with a sharp Cube orientation from annealing may lead to reduced earing behavior of CC Al-Mn-Mg alloy sheet products during deep drawing applications.

I. INTRODUCTION

AL-MN-MG (AA 3XXX) alloys are widely used as rigid can body materials that undergo deep drawing from circular sheet blanks. Upon completion of the drawing process, the top rim of the formed cups is not completely flat, but rather has undulations or ''ears''. This earing behavior is undesirable since more material must be trimmed from the top of the can, which requires an additional processing step and leads to material waste. It has been well established that earing behavior results from planar anisotropy and therefore crucially correlates with crystallographic texture formed during thermomechanical processing (TMP) of sheet products.[1–4] For aluminum alloys, earing behavior usually falls into one of two major types: (1) 45-deg earing (ears are formed 45 deg away from rolling direction [RD]), associated with the rolling texture components along the β fiber such as the Brass orientation {011}<211>, S orientation {123}<634>, and Copper orientation {112}<111>, and (2) 0-deg/90-deg earing (ears are formed in the RD and/or 90 deg away from the RD, also known as transverse direction [TD]) associated primarily with the Cube orientation {001}<100> and other recrystallization texture components such as the Goss orientation {011}<100>, Rotated (R)-Cube$_{RD}$ orientation {0kl}<100>, R-Cube$_{\text{normal direction (ND)}}$ orientation {001}<uv0>, and R-Cube$_{TD}$ orientation {0kl}<0vw>.

To obtain proper strength levels, aluminum can body sheets are typically produced under a H19 temper condition that involves heavy cold rolling (CR) reduction and results in a dominant deformation texture. Thus, 45-deg earing typically occurs. However, if a Cube texture can be introduced to counterbalance the deformation texture, then the final sheet products may have isotropic elongation properties. Therefore, securing a Cube texture may result in reduced earing behavior and significant cost savings.

At present, aluminum can body sheet products are usually manufactured by conventional direct chill (DC) cast ingots. Compared with DC cast technology, continuous cast (CC) technology takes advantages of both energy and economic savings while reducing environmental emissions. However, aluminum sheet products manufactured by the CC technology have been reported to possess poor recrystallization behavior (*i.e.*, difficult to be recrystallized, non-equiaxed grain structure) and high anisotropic properties due to high solute super-saturations resulting from the high cooling rate.[5,6] Additionally, it is difficult to secure a strong Cube texture to counterbalance the deformation texture. As a result, a high 45-deg earing tendency usually remains in the final CC aluminum sheet products, which is the major hurdle for using CC aluminum alloys as can body sheet.

In the past several decades limited efforts have been made to fabricate aluminum can body sheet using CC technology,[5] from which the foremost difficulty acknowledged resides in obtaining a strong Cube texture before the final CR to reduce earing behavior. A preliminary study[7] found that the major recrystallization texture of a CC Al-Mn-Mg alloy sheet was the P orientation {011}<566>. In an effort to modify the poor recrystallization behavior of the CC Al-Mn-Mg alloy sheet products during CR and subsequent annealing, an intermediate heat treatment (IHT) was introduced to homogenize the hot-rolled sheet products. The objective of this work was to study the microstructural and crystallographic textural development of cold-rolled and subsequently annealed CC Al-Mn-Mg alloy sheet products both with and without the IHT.

JIANTAO LIU, Senior Engineer, is with Alcoa Technical Center, 100 Technical Drive, Alcoa Center, PA 15069-0001. Contact e-mail: jiantao.liu@alcoa.com S.W. BANOVIC, Materials Research Engineer, is with the Metallurgy Division, Material Sciences and Engineering Laboratory, National Institute of Standards and Technology, Gaithersburg, MD 20899-8553. R.J. FIELDS, formerly Metallurgist with the Metallurgy Division, Material Sciences and Engineering Laboratory, National Institute of Standards and Technology, Gaithersburg, MD 20899-8553, is now retired. J.G. MORRIS, Professor Emeritus, is with the Department of Chemical & Materials Engineering, University of Kentucky, Lexington, KY 40506-0046.

Manuscript submitted February 25, 2005.

II. EXPERIMENTAL PROCEDURES

A. *Materials and Procedures*

Commercial CC Al-Mn-Mg alloy hot-rolled sheet products were used. Table I gives the chemical composition of the alloy used in this study. The hot-rolled sheet specimens were cut to dimensions of 3.6 × 68.0 × 116.0 mm^3 (Figure 1, normal direction [ND] × transverse direction [TD] × rolling direction [RD]) and then divided into two groups. Specimens from group 1 followed a processing route in which the IHT was *not* performed. As shown in Figure 2, the specimens were homogeneously cold rolled to 70 pct ($\varepsilon = 1.20$), 80 pct ($\varepsilon = 1.61$), and 90 pct ($\varepsilon = 2.30$) thickness reductions and then annealed isothermally at temperatures of 623 K, 723 K, and 823 K for 1800 s, followed by a water quenching. Specimens from group 2 followed the same CR and annealing processes as described above for the specimens from group 1 but received an IHT process prior to CR (Figure 2). The IHT process started with a homogenization at 893 K for 86,400 s, cooling to 823 K with a cooling rate 4.7×10^{-3} K/s, followed by another stage of homogenization at 823 K for 86,400 s, and then finished with a water quenching. The purpose of the IHT was to relieve the super-saturation status retained in the hot-rolled sheet specimens through precipitation and growth of the dispersoids.

B. *Microstructures*

Samples for microstructure examination were cut on ND-RD planes (refer to specimen geometry in Figure 1). The examined surface was prepared to 1 μm alpha alumina using standard metallographic procedures. The samples were then electropolished at a voltage of 27 V D.C. for 3 s using 15 mL HNO_3−50 mL $HClO_4$−950 mL CH_3OH followed by anodizing at a voltage of 18 V D.C. for 60 s using Barker's reagent (50 mL HBF_4−950 mL H_2O). The microstructure of anodized samples was examined using optical microscopy with polarized light. The second-phase morphology was determined using backscattered electron imaging on a JEOL* JSM-5900 LV scanning electron microscope (SEM).

*JEOL is a trademark of Japan Electron Optics Ltd., Tokyo.

C. *Electrical Resistivity*

Electrical resistivity of the specimens was measured based on the eddy current method according to ASTM E 1004[8] using a SIGMASCOPE** SMP 1 made by Fischer Instrumentation. Five measurements were made randomly for each specimen. The average of these five measurements was used as the final result of the specimen measured.

**SIGMASCOPE is a trademark of Fischer Instrumentation (GB) Ltd., Hampshire, U.K.

D. *Textures*

The macrotextures were measured at the half-thickness layer by the Schulz reflection method[9] on a Rigaku D/MAX X-ray goniometer using Cu K_α radiation. The goniometer was operated at 40 kV and 20 mA. The beam was reflected off of planes parallel to the rolling plane (RD-TD plane). Three incomplete pole figures {111}, {200}, and {220} ($0 \text{ deg} \le \alpha \le 75 \text{ deg}$) were measured and subsequently corrected for defocusing errors and background intensity. The spherical harmonic analysis[10] was used to calculate complete pole figures from the three incomplete pole figures. From these complete pole figures, three-dimensional orientation distribution functions (ODFs) $f(g)$ were calculated using Williams-Imhof-Matthies-Vinel (WIMV) method.[11,12] The preferred orientation package Los Alamos (*popLA*)[13] was used for all macrotexture analyses in this study. Three-dimensional ODFs were presented in Euler space defined by the three Euler angles ϕ_1, Φ, and ϕ_2 with the range of $0 \le \phi_1, \Phi, \phi_2 \le 90$ deg.[10] Two-dimensional ODFs were plotted in the format of iso-intensity contour lines within constant ϕ_2 sections through the above-mentioned Euler space with $\Delta\phi_2 = 5$.

Microtextures of planes parallel to the ND-RD plane, presented in the form of orientation maps, were obtained using a JEOL 6400 SEM equipped with CHANNEL 5 electron backscatter diffraction (EBSD) system from HKL Technology. The SEM operated at 20 kV with a probe current of 1×10^{-7} A. The specimen was tilted at an angle of 68 deg. Step size of the maps was 1 μm. Three map scans were performed over different areas of each specimen to ensure the statistical reliability of the data. The total number of data points for each map scan was more than 100,000.

III. RESULTS

A. *Microstructures of Al-Mn-Mg Alloy*

1. *As-received hot-rolled sheet*

Figure 3 shows microstructures of the as-received hot-rolled CC Al-Mn-Mg alloy sheet. The microstructure had severely elongated grain structures in the RD (Figure 3(a)), which is typical for hot-rolled aluminum alloys. It was evident that the second-phase particles also tended to align preferentially along the RD (Figure 3(b)). The major second-phase particles in Al-Mn-Mg alloys were most likely $Al_6(Fe,Mn)$, $Al_{12}(Fe,Mn)_3Si$, and Mg_2Si.[14–18]

2. *As-received hot-rolled sheet with the IHT*

After the IHT, the recrystallized grains were still significantly elongated in the RD (Figure 4(a)). It should be emphasized that a complete recrystallization status has been achieved after the IHT based on microhardness measurements.[6] Compared with the as-received sheet specimen

Table I. Chemical Compositions of the Al-Mn-Mg Alloy in the Present Study

Alloy	Mn	Mg	Cu	Fe	Si	Zn	Cr	Ni	Ti	Al
Al-Mn-Mg	0.52	0.46	0.20	0.74	0.35	0.16	0.37	0.01	0.02	Balance

Data are given as mass fractions multiplied by 100.

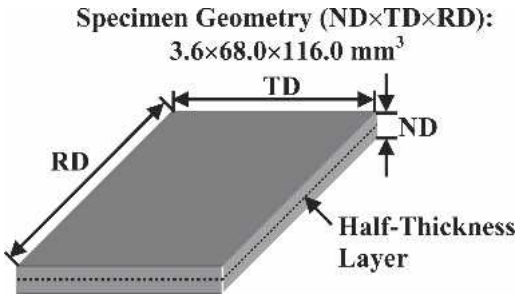

Fig. 1—Specimen geometry of as-received CC Al-Mn-Mg alloy hot-rolled sheet.

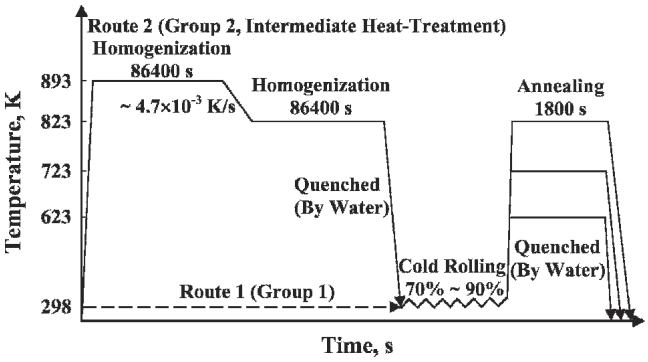

Fig. 2—Schematic map of TMP routes of as-received CC Al-Mn-Mg alloy hot-rolled sheet. Route 1 (dashed line) involved only CR and annealing, while route 2 (solid line) included an IHT prior to the same CR and annealing as illustrated in route 1.

(Figure 3(b)), the sheet specimen with the IHT appeared to contain coarser second-phase particles (Figure 4(b)), but no quantitative comparison was made. Measurements of the electrical resistivity showed that the electrical resistivity slightly decreased from 3.84 $\mu\Omega$-cm (standard deviation: $\pm$0.006 $\mu\Omega$-cm) for the as-received sheet specimen to 3.79 $\mu\Omega$-cm (standard deviation: $\pm$0.004 $\mu\Omega$-cm) for the sheet specimen after the IHT. It has been well established that metals in solid solution tend to increase the resistivity of an alloy to a greater extent than when they precipitate out of solution.[19] Therefore, the decrease in electrical resistivity suggests that more particles precipitated after the IHT.

3. *Cold-rolled sheet*

Figure 5 shows the grain structure of specimens from both groups after 70 pct CR reduction. A typical pancake grain structure was developed in which the grains were significantly deformed in the RD for both group 1 without the IHT (Figure 5(a)) and group 2 with the IHT (Figure 5(b)). There was no discernable difference between the two microstructures, with the exception that the specimens from group 2 appear to have undergone a less degree of deformation based on the dimension of grains in the ND. This difference was not surprising, as a completely recrystallized structure was achieved for specimens from group 2 prior to CR.

4. *Cold-rolled sheet after annealing*

The specimen from group 1 (without the IHT) showed a significantly elongated grain structure in the RD (Figure

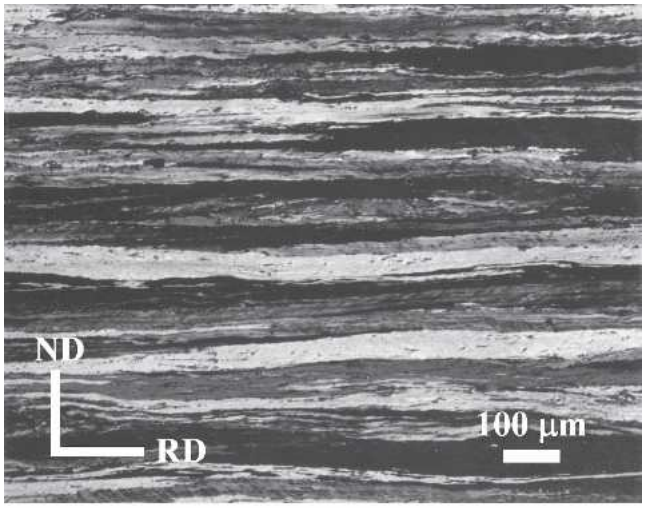

(*a*)

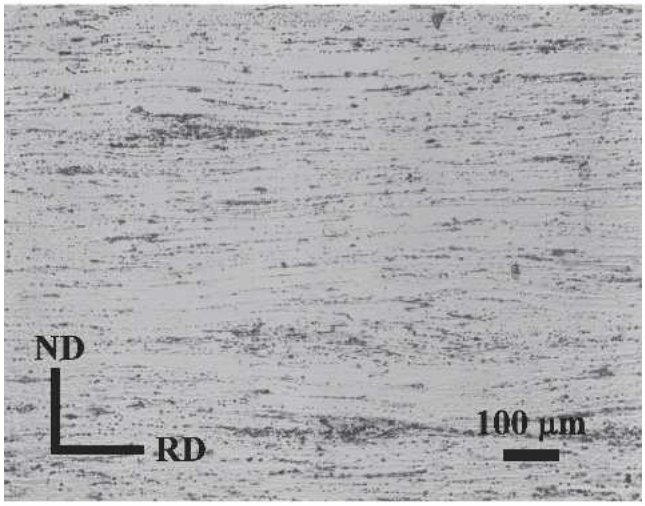

(*b*)

Fig. 3—Microstructure of the as-received CC Al-Mn-Mg alloy sheet: (*a*) a polarized light optical micrograph of grain structure and (*b*) a reflected light micrograph of second-phase particle structure.

6(a)) after 70 pct CR followed by annealing. In contrast, the similarly processed specimen from group 2 (with the IHT) showed a more equiaxed recrystallization grain structure (Figure 6(b)). This difference was also observed for the annealed specimens with 90 pct CR reduction (Figures 6(c) and (d)). However, the recrystallization grain size for both groups was refined under the higher CR reduction. The second-phase particle morphology of the annealed specimens shown in Figures 6(c) and (d) can be seen in Figures 7(a) and (b), respectively. The second-phase particles were somewhat more preferentially aligned parallel to the RD in the annealed specimen without the IHT (Figure 7(a)) than those in the specimen from group 2 with the IHT (Figure 7(b)).

B. *Textures of Al-Mn-Mg Alloy*

1. *As-received hot-rolled sheet*

Figure 8 presents the macrotexture of the as-received sheet. The {111} pole figure (Figure 8(a)) indicated a typical

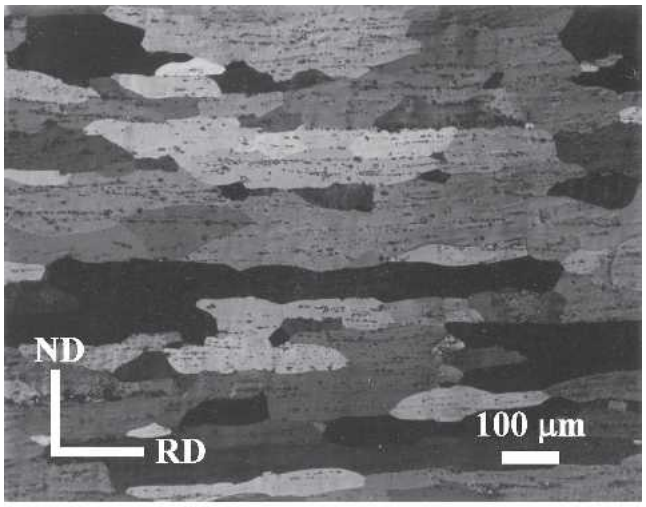

(*a*)

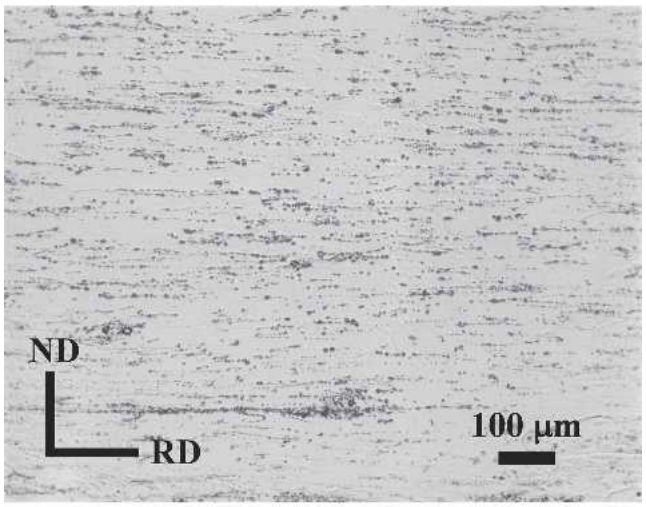

(*b*)

Fig. 4—Microstructure of as-received CC Al-Mn-Mg alloy sheet after IHT: (*a*) a polarized light optical micrograph of grain structure and (*b*) a reflected light micrograph of second-phase particle structure.

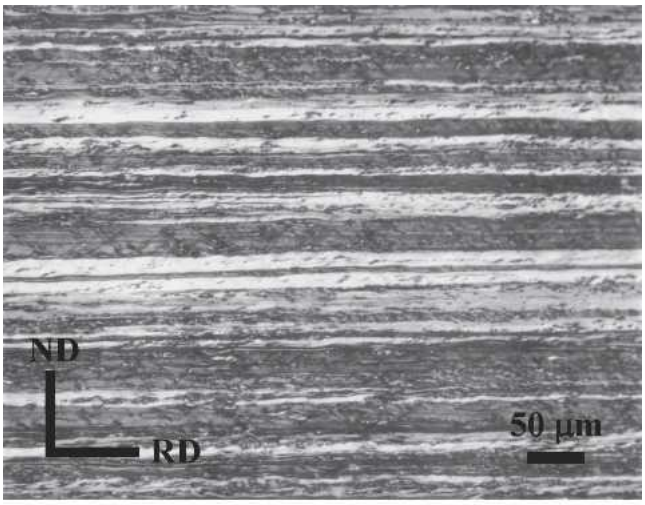

(*a*)

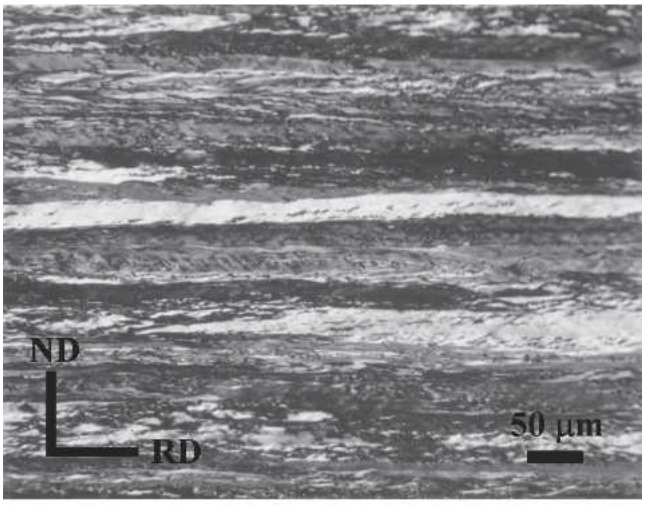

(*b*)

Fig. 5—Polarized light optical micrographs of CC Al-Mn-Mg alloy sheet after (*a*) 70 pct CR and (*b*) IHT and 70 pct CR.

rolling texture for fcc metals with high stacking fault energy (SFE). The three-dimensional ODF (Figure 8(b)) showed a well-developed β fiber that extended from the Copper orientation {112}<111> through the S orientation {123}<634> to the Brass orientation {011}<211>. The two-dimensional ODF (Figure 8(c)) showed that the highest intensity along the β fiber was located at the S orientation {123}<634>.

2. *As-received hot-rolled sheet with the IHT*

The macrotexture measurement of the sheet after the IHT was unsuccessful since the grains grew to such an extent that most X-ray reflections originated from only a few grains. As a result, the measurement resulted in a loss of the statistical feature of the macrotexture. Previous work[6] showed that most of the RD-elongated recrystallized grains in the partially recrystallized hot-rolled sheet are of the {011}<233> orientation that is close to the P orientation {011}<566>.

3. *Cold-rolled sheet*

The ODFs, at sections of $\phi_2 = 45$ deg, $\phi_2 = 65$ deg, and $\phi_2 = 90$ deg, are presented in Figure 9 for both groups of specimens with reductions of 70 pct, 80 pct, and 90 pct. The ODFs of all specimens from group 1 (Figure 9(a)) showed a well-developed β fiber that stemmed from the Copper orientation {112}<111> through the S orientation {123}<634> to the Brass orientation {011}<211>. The intensity of the Copper orientation increased from 13.1 after 70 pct CR to 20.0 after 90 pct CR. It is interesting to note that the intensity of the S orientation decreased from 18.2 after 70 pct CR to 15.3 after 90 pct CR. The intensity of the Brass orientation remained almost constant for the different CR reductions. The ODFs of specimens from group 2 (with the IHT) are shown in Figure 9(b). In general, the ODFs appear similar when compared to the as-received sheet but have less intensity and were more scattered. A weak Cube orientation {001}<100> was observed to be retained after 70 pct CR but was not observed for the 80 pct and 90 pct CR.

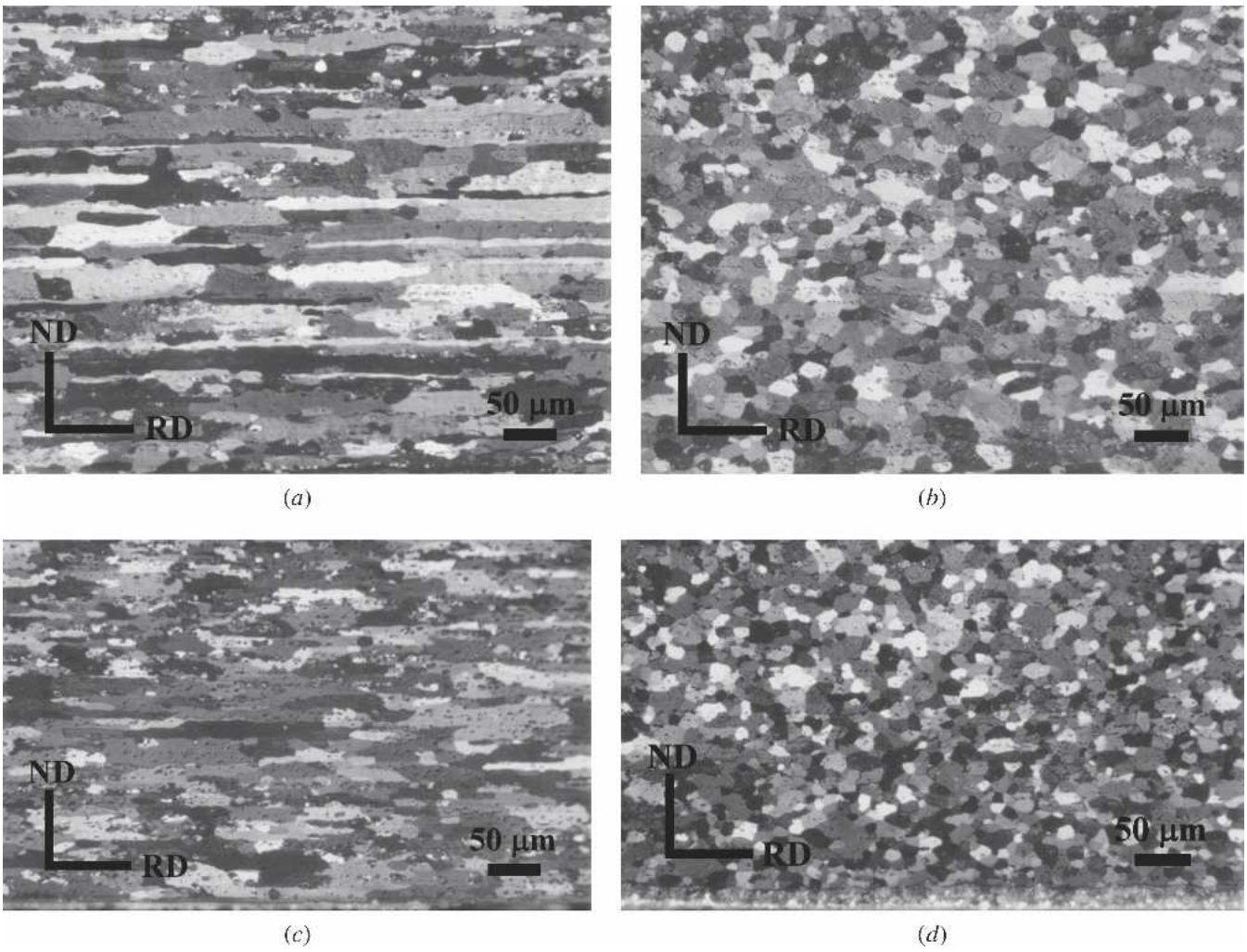

Fig. 6—Polarized light optical micrographs of CC Al-Mn-Mg alloy sheet after (*a*) 70 pct CR followed by annealing at 723 K for 1800 s, (*b*) IHT and 70 pct CR followed by annealing at 723 K for 1800 s, (*c*) 90 pct CR followed by annealing at 723 K for 1800 s, and (*d*) IHT and 90 pct CR followed by annealing at 723 K for 1800 s.

4. *Cold-rolled sheet after annealing*

Figure 10 shows the ODFs of the specimens following the annealing at 723 K for 1800 s. The ODFs shown in Figures 10(a) through (d) correspond to grain structures shown in Figures 6(a) through 6(d), respectively. After annealing at 723 K for 1800 s, the ODF of the 70 pct CR specimen from group 1 (Figure 10(a)) displayed a combination of textures consisting of both deformation (Copper {112}<111>, S {123}<634>, and Brass {011}<211>) and recrystallization (R-Cube$_{ND}$ {001}<130>, P {011}<566>, and Cube {001}<100>) orientations. This ODF result indicated a partial recrystallization status of the specimen. When compared to the ODF after cold rolling (Figure 9(a), 70 pct CR), the deformation textures were significantly weakened while the recrystallization textures developed. In contrast, for similar specimens with the IHT, the ODF exhibited a typical recrystallization texture with the Cube orientation {001}<100> as the major component (Figure 10(b)). Compared with the ODF of the cold-rolled specimen (Figure 9(b), IHT followed by 70 pct CR), the ODF of the annealed specimen remained nearly unchanged, with the exception of the weakened Copper orientation {112}<111> and development of the Cube orientation {001}<100>. The recrystallization textures (Figures 10(c) and (d)) of specimens with higher CR reduction (90 pct CR) became sharper and more intense. A strong P orientation {011}<566> accompanied by a weak R-Cube$_{ND}$ {001}<130> orientation developed in the specimen from group 1 (Figure 10(c)). In contrast, a strong Cube orientation {001}<100> was obtained in the specimen from group 2 (Figure 10(d)).

Figure 11 shows the orientation maps of annealed specimens with 70 pct CR. For the annealed specimen with 70 pct CR from group 1, many of the grains had a dimension in the RD that is 10 times greater than in the ND (Figure 11(a)). On the other hand, when annealed at the same conditions, the annealed specimen with 70 pct CR from group 2 exhibited a more equiaxed recrystallization grain structure (Figure 11(b)). Most of the elongated grains in the annealed specimen with 70 pct CR from group 1 formed either {001} or {011} texture.

Figure 12 displays the $\phi_2 = 0$ deg sections of the ODFs of the specimens at different CR reductions and annealing temperatures. The ODFs of the annealed specimens from

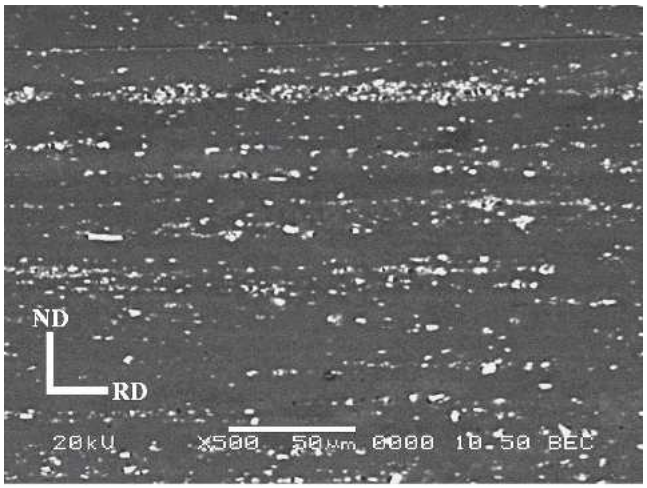

(*a*)

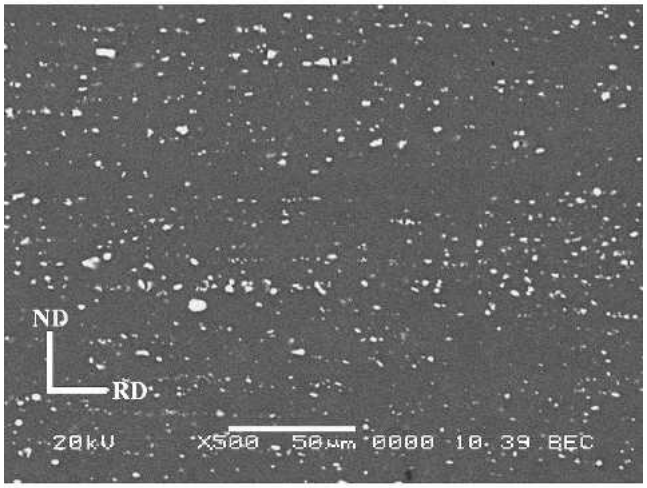

(*b*)

Fig. 7—SEM backscatter electron (BSE) micrographs showing second-phase particle structures in CC Al-Mn-Mg alloy sheet after (*a*) 90 pct CR followed by annealing at 723 K for 1800 s and (*b*) IHT and 90 pct CR followed by annealing at 723 K for 1800 s.

group 1 are shown in Figure 12(a). When annealed at 623 K, the specimen with 90 pct CR was the only one to develop the R-Cube$_{ND}$ orientation {001}<130>, indicating the start of recrystallization. The orientation proceeded to spread from the Brass orientation {011}<211> to the P orientation {011}<566>, which followed the trend observed in the specimen that was partially recrystallized (Figure 10(a)). It was clear that with increasing CR reduction prior to annealing, the P orientation {011}<566> became stronger and sharper. Figure 12(a) also indicates that the highest intensity of the P orientation {011}<566> was obtained in the 90 pct cold-rolling specimen after subsequent annealing at 723 K. However, the intensity of the P orientation {011}<566> decreased when the annealing temperature reached 823 K. The ODFs of the annealed specimens from group 2 (Figure 12(b)) were different compared to those from group 1 (Figure 12(a)). All specimens annealed at 623 K were already recrystallized. The Cube orientation {001}<100>, slightly rotated around the ND, developed as the major recrystallization texture in all specimens. The intensity of the Cube orientation {001}<100> increased with increasing CR reduction prior to annealing and also with increasing annealing temperature. The P orientation {011}<566> was nearly absent in all specimens.

IV. DISCUSSION

This work demonstrated that the IHT altered the development of both the microstructure and crystallographic texture of the CC Al-Mn-Mg hot-rolled sheet during CR and subsequent annealing. Moreover, the CR reduction prior to annealing and the annealing temperature were important in determining the microstructure and texture of the final sheet product. The following section discusses the effect of each processing condition in detail.

A. *Effect of the IHT on Microstructure and Texture Evolution: Key Factor*

Subsequent to annealing, the specimens of group 1 (cold rolled directly from the as-received, hot-rolled, CC Al-Mn-Mg sheet) acquired an elongated recrystallization grain structure (Figures 6(a) and (c)). Crystallographically, this grain structure was associated with the development of the P orientation {011}<566> and the R-Cube$_{ND}$ {001}<130> orientation (Figures 10(a), (c), and 12(a)). This development is typical for CC Al-Mn-Mg alloys.[20,21,22] In contrast, the specimens of group 2 (undergoing an IHT before CR) obtained an equiaxed grain structure (Figures 6(b) and (d)) and developed a Cube orientation {001}<100> (Figures 10(b), (d), and 12(b)). This microstructure and texture result suggests a completely different recrystallization behavior from that observed in specimens from group 1. The difference in recrystallization behavior was attributed to the IHT that altered the super-saturation status of the as-received CC Al-Mn-Mg sheet, and consequently the morphology of the second-phase particles.

For Al-Mn-Mg alloys, a bimodal distribution of second-phase particles, consisting of coarse primary intermetallic particles formed at the solidification stage and a dispersion of fine secondary particles precipitated during later TMP, may exist.[14–17] The coarse particles have been shown to have no effect on the recrystallization behavior of the material. However, previous investigations have shown that the fine secondary Fe- and Mn-bearing precipitates,[23] particularly Al_6Mn,[24,25] have a critical impact on the recrystallization behavior of Al-Mn-Mg alloys. It has been well recognized that the second-phase particles may either accelerate or retard recrystallization, depending on the type, size, and distribution of the precipitates.[26] As an example, large particles (>1 μm) may provide nucleation sites and stimulate recrystallization (particle-stimulated nucleation [PSN]), while the smaller, more closely spaced particles may have a pinning effect on grain boundaries (Zener drag). Zener drag that occurs during recrystallization comes from two sources: (1) the drag from particles precipitating on the substructure or moving boundaries and (2) the drag from particles precipitated during earlier processing or constituent particles during casting.[27]

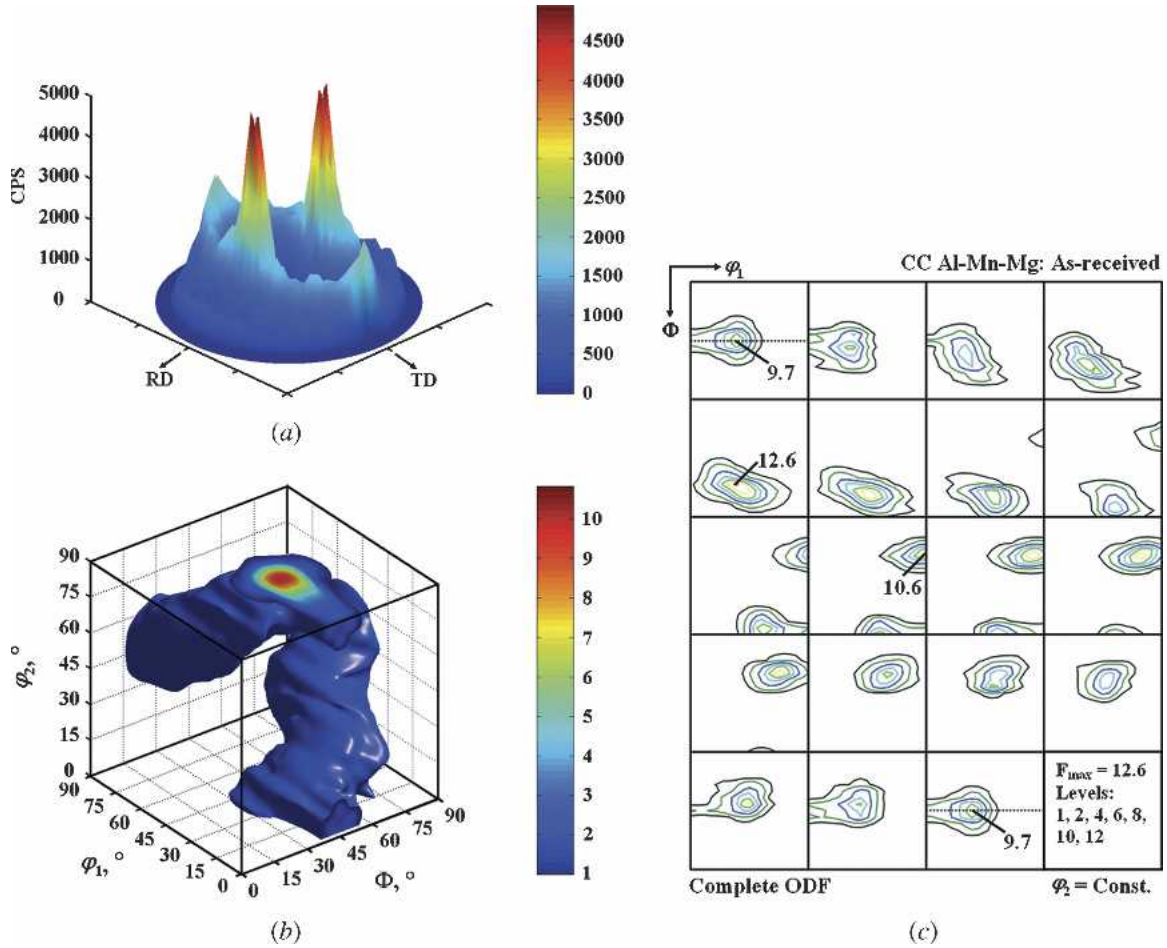

Fig. 8—Macrotexture of as-received CC Al-Mn-Mg alloy sheet: (*a*) measured {111} incomplete pole figure, (*b*) calculated three-dimensional ODF, and (*c*) two-dimensional contour plot in constant sections (constant ϕ_2 sections with $\Delta\phi_2 = 5$ deg) of the ODF shown in (*b*).

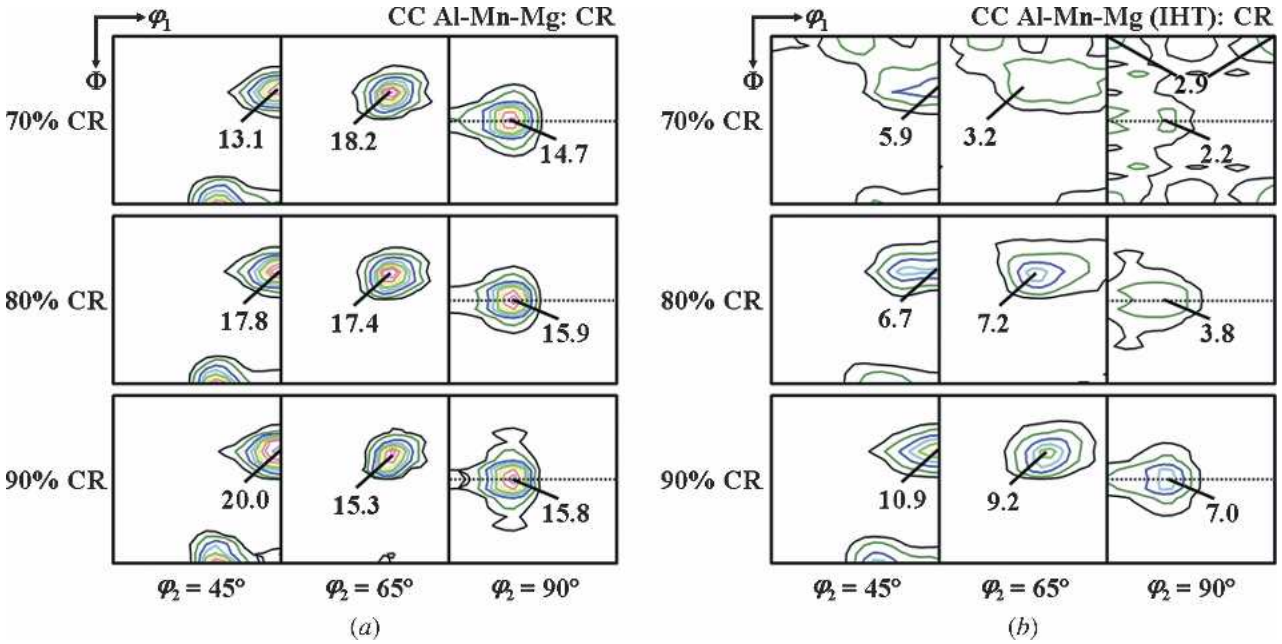

Fig. 9—ODFs at sections of $\phi_2 = 45$ deg, $\phi_2 = 65$ deg, and $\phi_2 = 90$ deg of CC Al-Mn-Mg alloy sheets (*a*) without IHT and (*b*) with IHT after 70 pct, 80 pct, and 90 pct CR.

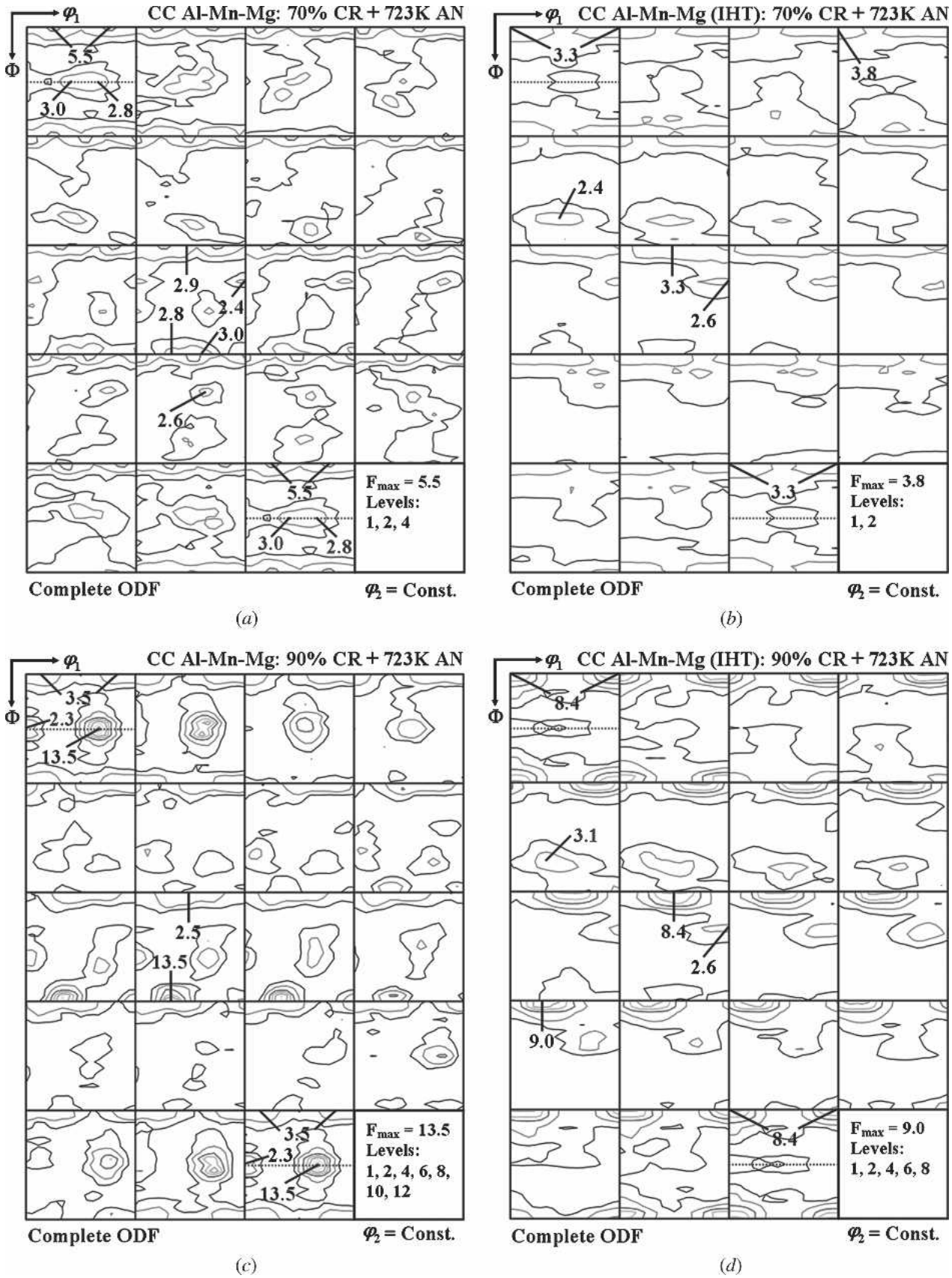

Fig. 10—ODFs of the four microstructures shown in Figure 6 for the CC Al-Mn-Mg alloy sheet after (*a*) 70 pct CR followed by annealing at 723 K for 1800 s, (*b*) IHT followed by 70 pct CR and annealing at 723 K for 1800 s, (*c*) 90 pct CR followed by annealing at 723 K for 1800 s, and (*d*) IHT followed by 90 pct CR and annealing at 723 K for 1800 s.

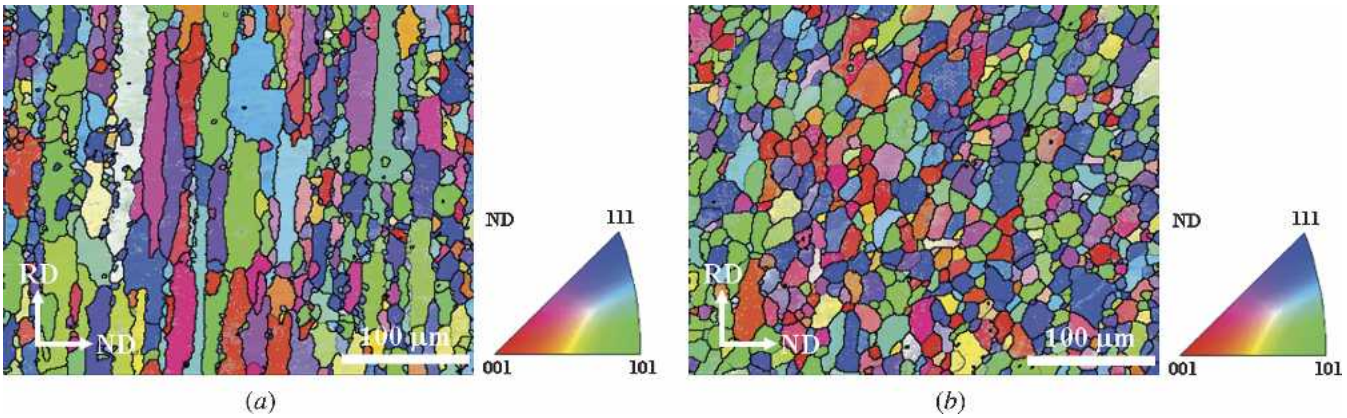

Fig. 11—EBSD orientation maps of CC Al-Mn-Mg alloy sheet after (*a*) 70 pct CR followed by annealing at 723 K for 1800 s and (*b*) IHT followed by 70 pct CR and annealing at 723 K for 1800 s. The colors of grains correspond to the crystal orientations shown in the inverse pole figure triangle legends.

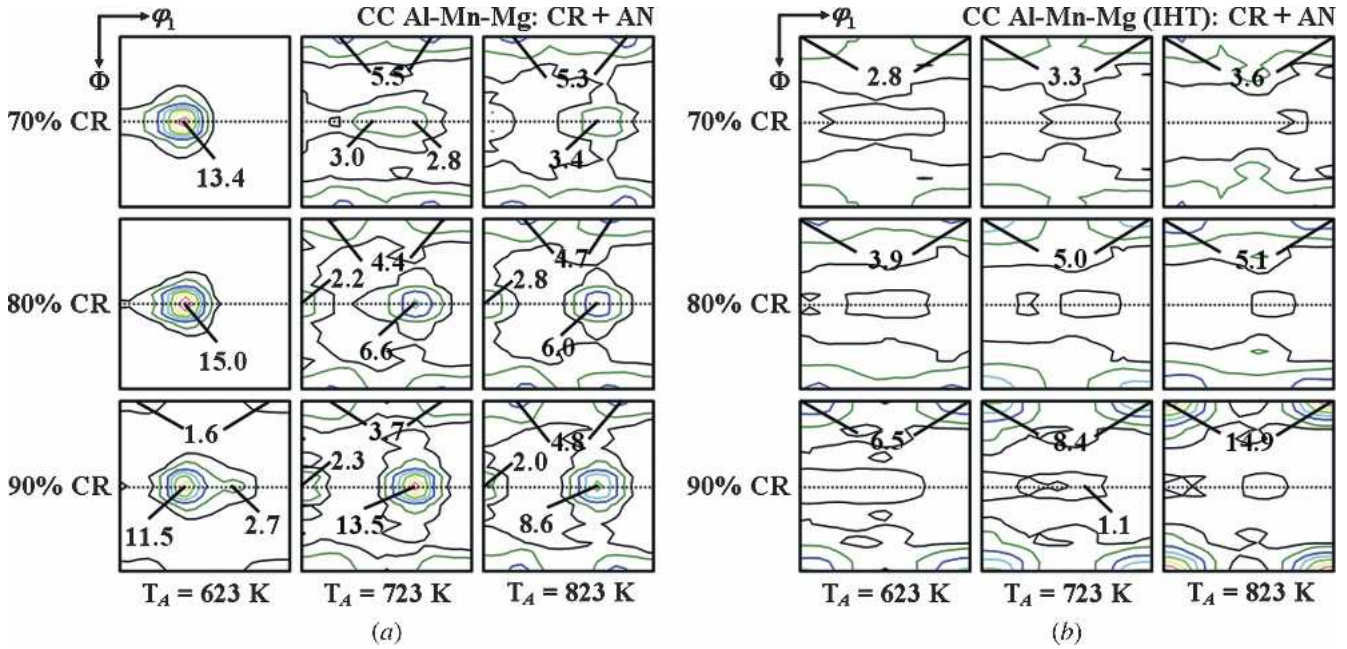

Fig. 12—ODFs at section of $\phi_2 = 0$ deg of CC Al-Mn-Mg alloy sheets after (*a*) 70 pct, 80 pct, and 90 pct CR followed by annealing at temperatures of 623 K, 723 K, and 823 K for 1800 s and (*b*) IHT followed by 70 pct, 80 pct, and 90 pct CR and annealing at temperatures of 623 K, 723 K, and 823 K for 1800 s.

The specimens from group 1 processed without the IHT developed a highly RD-elongated grain structure after CR and annealing because of the retained super-saturation status. As a result, CR and annealing may have resulted in a concurrent precipitation process (*i.e.*, precipitation occurred concurrently with recrystallization) that retarded the recrystallization process. This behavior can be observed in specimens from group 1, demonstrating the delayed development of recrystallization textures (Figure 12(a) *vs* Figure 12(b)).

It is well accepted that Fe- and Mn-bearing second-phase precipitates are responsible for altering recrystallization behavior when they precipitate simultaneously with ongoing recrystallization.[28,29] In previous work,[7] fine Al_6Mn precipitates were found in specimens from group 1 after CR followed by annealing. However, it was difficult to identify the effect from certain precipitates on recrystallization behavior, since the precipitating reaction of the commercial Al-Mn-Mg alloys was too complicated to identify, even though significant efforts have been made in the past.[30,31] It was reported that particles develop in bands on the rolling plane and lead to highly RD-elongated recrystallization grain structure in Al-Mn alloy sheet.[32] It was further demonstrated that the migration rate of grain boundaries in the ND could be virtually zero during the final stage of recrystallization, which is attributed to Zener drag from non-random particle distribution. It is not known whether closely spaced constituents in the RD (Figure 7(a)) restrict the grain boundary migration in the ND and therefore contribute to the highly RD-elongated recrystallization grain structure or not. Zener drag from non-random particle distribution appears to be able to explain the highly RD-elongated recrystallization grain structure in the following

way. Second-phase particles tended to align preferentially along the RD and led to a weaker Zener pinning effect of grain boundaries in the RD compared with that in the ND. As a result, banded second-phase particles along the RD significantly restricted the migration of grain boundaries and led to a much smaller growth rate in the ND than in the RD. However, the influence of conditions such as the type and size of particles, grain boundary characteristics after rolling strain, *etc*., on the formation of the highly RD-elongated recrystallization grain structure is not yet completely understood.

On the other hand, the super-saturation status in the specimens from group 2 was relieved by the IHT. This relief of super-saturation status resulted in a coarser second-phase particle structure (Figure 4(b)) as compared to that of specimens in group 1 (Figure 3(b)). Therefore, concurrent precipitation was weakened during further CR and annealing processes as the driving force for particle precipitation had dramatically decreased. As a result, the sheet with the IHT was observed to recrystallize at a much faster rate compared with the specimens from group 1. This difference in recrystallization was verified by the microstructural development (Figure 6(a) *vs* (b)) and texture results (Figure 12(a) *vs* (b), T_A = 623 K). The electrical resistivity of the as-received sheet also decreased by 0.05 $\mu\Omega$-cm after the IHT, suggesting that more particles precipitated as a result of the IHT. A more uniform dispersion of second-phase particles formed during the subsequent CR and annealing for the specimens from group 2 (Figure 7(b)) than observed for those from group 1 (Figure 7(a)). It is also possible that the distribution of the second-phase particles was important in affecting the recrystallization behavior. The dispersive second-phase particle structure with coarse precipitates (>1 μm) is believed to promote PSN during recrystallization,[33] which favors the formation of the equiaxed grain structure.

The formation of the P orientation {011}<566> has been reported in pure Al,[34] Al-Cu alloy,[35] Al-Mn,[36–39] and Al-Fe-Si[40] alloys. Engler *et al.*[37,41] proposed that the P orientation {011}<566> and the R-$Cube_{ND}$ orientation {001}<130> can be attributed to a PSN mechanism: nucleation that occurs by rapid subgrain growth within the deformation zones around the large particles (>1 μm). During the early stages of annealing, some growth preference of the P and R-$Cube_{ND}$ orientations takes place (micro-growth selection), which eventually results in the development of these orientations. It has been pointed out[34] that the PSN grains cannot grow sufficiently so as to dominate the recrystallization texture. Thus, it seems difficult to explain the strong P orientation obtained in this study by a PSN mechanism. The origin of the recrystallization textures has been debated for decades between oriented nucleation (ON)[42] and oriented growth (OG)[43] theories. It is still not clear whether ON, OG, or both determine the formation of the P orientation. Limited results[38,39,40] have shown that a 40-deg <111> transformation from typical rolling texture with well-developed β fiber results in the P {011}<566> and R-$Cube_{ND}$ {001}<130> orientations, which appears to support the growth selection model during the growth of the nuclei. The origin of the Cube orientation {001}<100> is a subject that has been intensively studied as well as discussed[44,45] and is beyond the scope of this paper.

B. *Effect of the CR Reduction on Microstructure and Texture Evolution*

CR reduction prior to annealing had a significant effect on the development of both the microstructure and texture of the specimens studied in this work. In terms of the microstructural development, increased CR reduction prior to annealing yielded a finer recrystallization grain size (Figure 6) subsequent to the annealing step. This trend was observed for specimens from both groups (with and without the IHT), which can be attributed to a higher driving force for nucleation and concomitant nucleation rate of recrystallization grains, as a result of the higher degree of deformation.

CR was also found to have an effect on the texture evolution during subsequent annealing. For specimens from group 1, the P orientation {011}<566> became sharper and more intense with increased degree of CR reduction prior to annealing (Figures 10 and 12). This result can be explained by strain-induced precipitation that formed a very closely spaced, banded second-phase particle distribution at higher CR reductions, which further restricted the growth of the recrystallized grains during the annealing process, and as a result the intensity of the P orientation {011}<566> increased.

However, for specimens from group 2 that underwent the IHT, increasing the CR reduction prior to annealing strongly favored the formation of the Cube orientation {001}<100> during annealing (Figure 12(b)). It can be seen that the intensity of the Cube orientation {001}<100> was more than doubled regardless of annealing temperature when comparing the 70 pct and 90 pct cold-rolled specimens. Both ON and OG advantages of the Cube-oriented grains have been used to explain the dominant Cube orientation {001}<100> in recrystallization texture.[46] However, contradictory findings are typically presented. While Hjelen *et al.*[44] found that a 40-deg <111> relationship has no effect on the growth of the Cube orientation {001}<100>, Engler *et al.*[34] found that there exists 40-deg <111> growth preference for the Cube-oriented grains at high strains and high annealing temperatures. As shown in Figure 9(b), the intensity of the S orientation {123}<634> increased with an increase in CR reduction. It is also shown that the intensity of the Cube orientation {001}<100> increased with increasing CR reduction prior to annealing (Figure 12(b)). While these results seem to lend support to growth advantage of the Cube orientation, nucleation advantage of the Cube nuclei may not be excluded. Avoiding concurrent precipitation during CR and annealing seemed to favor the formation of the strong Cube orientation {001}<100>.

C. *Effect of Annealing Temperature on the Texture Evolution*

Figure 12 also displayed the effect of annealing temperature on the texture evolution. For the recrystallization textures of specimens from group 1 (Figure 12(a)), the intensity of the P orientation {011}<566> reached its peak value during annealing at 723 K. The intensity of the P orientation {011}<566>, however, was weakened when the annealing temperature was increased to 823 K. This

phenomenon can probably be attributed to the second-phase precipitation process during annealing. Annealing at 723 K resulted in the development of finer precipitates that led to a stronger Zener drag effect. However, annealing at 823 K coarsened the second-phase precipitates and thus weakened the Zener drag effect. Consequently, a weaker P orientation accompanied by a stronger R-Cube$_{ND}$ orientation {001}<130> was observed for all specimens annealed at 823 K.

For the specimens from group 2, the intensity of the Cube orientation {001}<100> increased with increasing annealing temperature during annealing (Figure 12(b)). At higher annealing temperatures, both nucleation rate and the growth of all orientations were generally accelerated. However, the Cube-oriented grains may take advantage of the growth preference that led to the stronger Cube orientation {001}<100> in the recrystallization textures.[34] As a result, a strong Cube orientation {001}<100> formed in specimens from group 2.

D. *Perspective on Findings*

A striking result of this work was that the IHT had a significant effect on the microstructure and texture evolution of the CC Al-Mn-Mg sheet. Applying the IHT on the hot-rolled sheet enhanced the development of the Cube texture {001}<100> and improved poor recrystallization behavior of the final CC Al-Mn-Mg sheet products. As a result, a strong Cube texture {001}<100> was secured for counterbalancing the rolling textures. Therefore, with an IHT process, high 45-deg earing behavior, the major technical hurdle of producing CC Al-Mn-Mg sheet for beverage can stock on a commercial scale, may be overcome. However, optimization of the IHT process is necessary to meet the requirements of commercial production.

In this work, we restricted our attention to presenting the significant impacts of the IHT on the CC Al-Mn-Mg hot-rolled sheet during subsequent TMP. Further TEM and EBSD work is imperative to understand the origin of the P orientation {011}<566>, which will provide insight into the mechanism of recrystallization behavior of CC aluminum alloys and may help to optimize the IHT process.

V. CONCLUSIONS AND SUMMARY

The effects of the IHT on the development of microstructure and crystallographic texture of CC Al-Mn-Mg hot-rolled sheet during subsequent CR and annealing were investigated. For the hot-rolled sheet specimens without the IHT, a severely elongated grain structure was found in which the texture was dominated by a strong P orientation {011}<566>, despite the fact that the specimen was completely recrystallized. In contrast, hot-rolled sheet specimens receiving the same CR and annealing conditions but with the IHT had an equiaxed grain structure with a sharp Cube orientation {001}<100>.

Additionally, CR reduction and subsequent annealing processes were observed to have a significant effect on the microstructure and texture of the CC Al-Mn-Mg sheet both with and without the IHT. It was shown that increasing the CR reduction prior to annealing refined the recrystallized grain size after annealing. The intensity of the P {011}<566> orientations increased with increasing CR reduction prior to annealing for the sheet without the IHT, while the Cube {001}<100> orientation increased for the sheet with the IHT. During the annealing process, the intensity of the P orientation {011}<566> obtained its peak value at 723 K for the sheet without the IHT. The intensity of the Cube orientation {001}<100> in the sheet with the IHT increased with increasing annealing temperature.

With an optimized IHT process and subsequent modification of the recrystallization behavior during TMP, the possibility of using CC Al-Mn-Mg sheet for beverage can stock on a commercial scale may be feasible.

ACKNOWLEDGMENTS

Financial support from the U.S. Department of Energy (under Contract No. DE-FC07-01ID14193) is gratefully acknowledged. The authors thank Dr. R.E. Sanders Jr., Dr. J.D. Bryant, Mr. R.E. Dick, and anonymous reviewers for their helpful comments on the manuscript. J.T.L. acknowledges that the major portion of this study was undertaken while he was a graduate student at University of Kentucky, Lexington, Kentucky, and the final part was made while he was a postdoctoral research fellow associated with the Materials Science and Engineering Laboratory (MSEL) at the National Institute of Standards and Technology (NIST), Gaithersburg, Maryland. J.T.L. and S.W.B. would like to dedicate this paper to their co-author R.J.F. to celebrate his retirement after a successful professional career of more than 35 years in MSEL at NIST.

Identification of any equipment or software is for the purpose of describing the experimental techniques and does not imply recommendation or endorsement by NIST, the Department of Commerce, or the U.S. Government, nor does it imply that the identified equipment or software is the best available.

REFERENCES

1. G.E.G. Tucker: *Acta Metall.*, 1961, vol. 9, pp. 275-86.
2. H. Inagaki: *Z. Metallk.*, 1991, vol. 82, pp. 361-72.
3. O. Daaland and E. Nes: *Acta Mater.*, 1996, vol. 44, pp. 1389-411.
4. O. Engler and S. Kalz: *Mater. Sci. Eng., A*, 2004, vol. A373, pp. 350-62.
5. S.E. Naess: in *Aluminum Alloys for Packaging*, J.G. Morris, H.D. Merchant, E.J. Westerman, & P.L. Morris, eds., TMS, Warrendale, PA, 1993, pp. 275-98.
6. J. Liu: Ph.D. Thesis, University of Kentucky, Lexington, KY, 2003.
7. J. Liu and J.G. Morris: *Metall. Mater. Trans. A*, 2003, vol. 34A, pp. 2029-32.
8. ''Metals Test Methods and Analytical Procedures,'' in *Annual Book of ASTM Standards*, 2001, ASTM International, West Conshohocken, PA, pp. 447-50.
9. L.G. Schulz: *J. Appl. Phys.*, 1949, vol. 20, pp. 1033-36.
10. H.J. Bunge: *Texture Analysis in Material Science,* Butterworths, London, 1982, pp. 1-41.
11. S. Matthies and G.W. Vinel: *Phys. Stat. Sol.* (*b*), 1982, vol. 112, pp. K111-K114.
12. S. Matthies and G.W. Vinel: *Phys. Stat. Sol.* (*b*), 1982, vol. 112, pp. K115-K120.
13. J.S. Kallend, U.F. Kocks, A.D. Rollett, and H.-R. Wenk: *Mater. Sci. Eng.*, 1991, vol. A132, pp. 1-11.
14. P.L. Morris and B.J. Duggan: *Metall. Sci.*, 1978, vol. 12, pp. 1-7.
15. P. Furrer and G. Hausch: *Metall. Sci.*, 1979, vol. 13, pp. 155-62.
16. N. Hansen and B. Bay: *Acta Metall.*, 1981, vol. 29, pp. 589-99.
17. D.J. Lloyd: *Metall. Sci.*, 1982, vol. 16, pp. 304-08.
18. S. Saimoto and R.G. Kamat: *Mater. Sci. Technol.*, 1992, vol. 8, pp. 869-74.

19. J.E. Hatch: *Aluminum: Properties and Physical Metallurgy*, American Society of Metals, Metals Park, OH, 1984, pp. 204-06.
20. Z. Li, C. Li, and J.G. Morris: in *Aluminum Alloys for Packaging*, J.G. Morris, H.D. Merchant, E.J. Westerman, and P.L. Morris, eds., TMS, Warrendale, PA, 1993, pp. 299-307.
21. S. Ding, X. Fan, and J.G. Morris: in *Aluminum Alloys for Packaging*, J.G. Morris, H.D. Merchant, E.J. Westerman, and P.L. Morris, eds., TMS, Warrendale, PA, 1993, pp. 237-50.
22. Y.L. Liu, Y. Liu, G. Liao, and J.G. Morris: *Aluminum Trans.*, 2000, vol. 2, pp. 97-106.
23. O. Daaland and E. Nes: *Acta Mater.*, 1996, vol. 44, pp. 1413-35.
24. H.E. Vatne, O. Engler, and E. Nes: *Mater. Sci. Technol.*, 1997, vol. 13, pp. 93-102.
25. M. Somerday and F.J. Humphreys: *Mater. Sci. Technol.*, 2003, vol. 19, pp. 20-29.
26. R.D. Doherty, D.A. Hughes, F.J. Humphreys, J.J. Jonas, D. Juul Jensen, M.E. Kassner, W.E. King, T.R. McNelley, H.J. McQueen, and A.D. Rollett: *Mater. Sci. Eng. A*, 1997, vol. 238, pp. 219-74.
27. S. Benum and E. Nes: *Acta Mater.*, 1997, vol. 45, pp. 4593-602.
28. R.D. Doherty and J.W. Martin: *J. Inst. Metals*, 1962, vol. 91, pp. 332-38.
29. E. Nes and J.D. Embury: *Z. Metallk.*, 1975, vol. 66, pp. 589-93.
30. R.G. Kamat: *J. Metall.*, 1996, vol. 48, pp. 34-38.
31. T.N. Rouns: in *Aluminum Alloys for Packaging III*, S.K. Das, ed., TMS, Warrendale, PA, 1998, pp. 3-20.
32. E. Nes, N. Ryum, and O. Hunderi: *Acta Metall.*, 1985, vol. 33, pp. 11-22.
33. F.J. Humphreys: *Acta Metall.*, 1977, vol. 25, pp. 1323-44.
34. O. Engler, H.E. Vatne, and E. Nes: *Mater. Sci. Eng.*, 1996, vol. A205, pp. 187-98.
35. O. Engler, J. Hirsch, and K. Lücke: *Acta Metall. Mater.*, 1995, vol. 43, pp. 121-38.
36. H.E. Vatne, O. Engler, and E. Nes: *Mater. Sci. Technol.*, 1995, vol. 13, pp. 93-102.
37. O. Engler, P. Yang, and X.W. Kong: *Acta Mater.*, 1996, vol. 44, pp. 3349-69.
38. K. Sjølstad, O. Engler, S. Tangen, K. Marthinsen, and E. Nes: *Mater. Sci. Forum*, 2002, vol. 396–402, pp. 463-68.
39. K. Sjølstad, O. Engler, S. Tangen, K. Marthinsen, and E. Nes: *Mater. Sci. Forum*, 2002, vol. 408–412, pp. 1471-76.
40. K. Lücke and O. Engler: *Mater. Sci. Technol.*, 1990, vol. 6, pp. 1113-30.
41. O. Engler: *Mater. Sci. Technol.*, 1996, vol. 12, pp. 859-72.
42. W.G. Burgers and P.C. Louwerse: *Z. Phys.*, 1931, vol. 67, pp. 605-78.
43. C.S. Barett: *Trans. AIME Metall. Engineering*, 1940, vol. 137, pp. 128-49.
44. J. Hjelen, R. Ørsund, and E. Nes: *Acta Metall. Mater.*, 1991, vol. 39, pp. 1377-404.
45. R.D. Doherty: *Acta Metall. Mater.*, 1993, vol. 41, pp. 3029-53.
46. J. Hirsch and K. Lücke: *Acta Metall.*, 1985, vol. 33, pp. 1927-38.